PAPER • OPEN ACCESS

Topology-optimized photonic topological crystalline insulators with multiband helical edge states

To cite this article: Yafeng Chen *et al* 2024 *New J. Phys.* **26** 083025

View the article online for updates and enhancements.

New Journal of Physics

The open access journal at the forefront of physics

PAPER

Topology-optimized photonic topological crystalline insulators with multiband helical edge states

Yafeng Chen[1,*] ⓘ, Zhihao Lan[2] ⓘ, Hai-Xiao Wang[3], Liang An[1] and Zhongqing Su[1]

[1] Department of Mechanical Engineering, Hong Kong Polytechnic University, Hong Kong Special Administrative Region of China, People's Republic of China
[2] Department of Electronic and Electrical Engineering, University College London, London WC1E 7JE, United Kingdom
[3] School of Physical Science and Technology, Ningbo University, Ningbo 315211, People's Republic of China
[*] Author to whom any correspondence should be addressed.

E-mail: yachen@polyu.edu.hk

Abstract

Photonic topological crystalline insulators (PTCIs) with helical edge states provide an alternative way to achieve robust electromagnetic wave transport and processing. However, most existing PTCIs only involve a single topological bandgap, and generally support a pair of gapped helical edge states, restricting the scope of applications in various fields such as multiband waveguides, filters, and communication systems. Here, we design dual-band PTCIs, in which multiple helical edge modes appear within two distinct bulk gaps, for transverse electric (TE) and transverse magnetic (TM) modes, respectively, by introducing the topology optimization method into the photonic crystals with glide symmetry. For PTCIs with TE modes, the mismatched frequency ranges of edge modes hosted by two orthometric boundaries offer an opportunity to realize a photonic demultiplexer. For PTCIs with TM modes, we show the enhanced second harmonic (SH) generation through the coupling of multiband edge modes by matching the frequency ranges of edge modes within the first and second bandgaps to fundamental and SH waves, respectively. This work provides a new way for designing multiband PTCIs with helical edge states, having promising potentials in developing multiband topological photonic devices for both linear and nonlinear applications.

1. Introduction

The invent of photonic topological insulators (TIs), featuring topologically protected edge states, has offered an unprecedented approach to steer electromagnetic waves, paving a new way for advanced photonic devices beyond traditional ones [1–11]. To date, multiple versions of photonic TIs based on different physical mechanisms have been created by mimicking TIs in condensed matter physics. Based on the quantum Hall effect, the earlier photonic TIs consisting of gyromagnetic photonic crystals (PCs) need to utilize external magnetic fields to break the time-reversal symmetry [12, 13], which, however, are incompatible with on-chip devices. To solve this problem, photonic topological crystalline insulators (PTCIs) with specific crystalline symmetry, which are made of all-dielectric materials, have been developed. One type of all-dielectric PTCIs is mimicking the quantum valley Hall effect (QVHE) [14, 15]. This is achieved by creating valley PCs via breaking the deterministic Dirac point to open a gap. Another type of all-dielectric PTCIs is the bosonic Z_2 topological crystalline insulator with pseudospin-locked helical edge modes, which are achieved by expanding and shrinking honeycomb lattices [16–18]. Such PTCIs host helical edge states, which can be exploited to develop novel pseudospin-locked photonic devices with robustness for both linear and nonlinear applications. However, such helical edge states are gapped due to the break of symmetry at the edge. Additionally, such as glide and screw symmetry, have been demonstrated as an effective method for realizing PTCIs with helical edge states [19–23]. These symmetries combine mirror/rotation symmetry with a translation operation. Furthermore, the traditional bulk-boundary correspondence has been expanded to
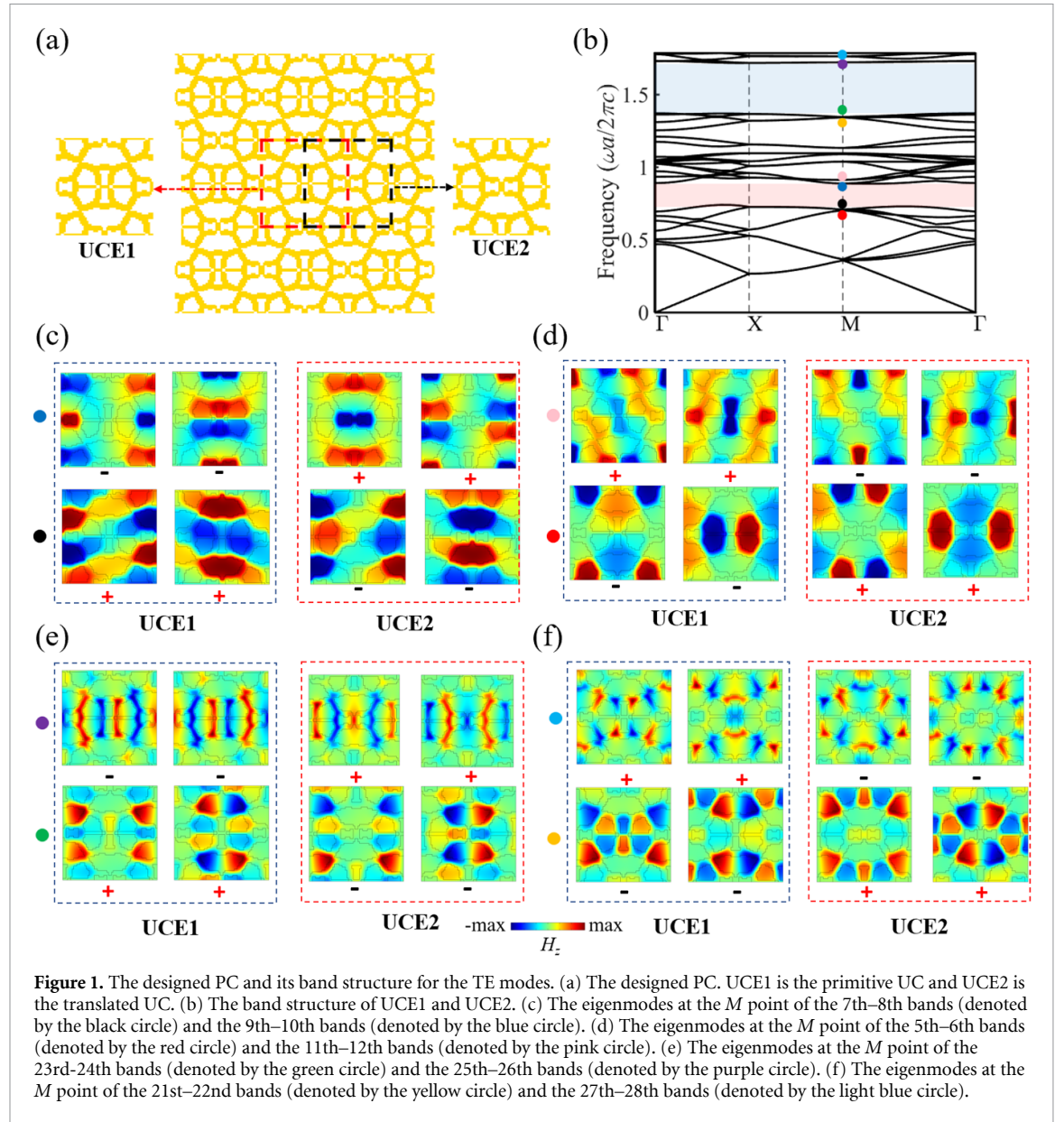
create a variety of high-order PTCIs. These PTCIs host both gapped edge modes and in-gap corner modes [24–28].

On the other hand, in the realm of integrated optics, multiband communication holds paramount importance for enhancing optical information processing capacity by encoding diverse signals into different wavelengths. Towards robust multiband communications, Chen *et al* [29] designed a PTCI hosting dual-band kink states. Thereafter, Lan *et al* successfully leveraged the dual-band kink states in a PTCI to achieve topologically protected second-harmonic generation [30]. Kim and Om developed a high-order PTCI that supports both multiband kink bands and second-order corner states [31]. Despite these advancements, the majority of these PTCIs are designed based on the QVHE and are primarily focused on multiband kink bands, whereas those host multiband pseudospin-locked helical edge states are less explored. Meanwhile, current multiband PTCIs based on QVHE are mainly designed based on physical intuition via trial-and-error, leading to the narrow bandwidth.

To overcome this challenge, we first apply the topology optimization method in PCs with glide and mirror symmetries to realize dual-bandgaps for transverse electric (TE) and transverse magnetic (TM) modes, respectively. Interestingly, the edge formed by placing two optimized PCs together, in which the unit cells (UCs) of two sides differ by a half lattice constant, supports two pairs of helical edge states within two bandgaps owing to the multiple band inversion mechanism. For PCTIs with TE modes, it is demonstrated that the frequency window mismatches of edge modes hosted by two orthogonal edges offer an interesting opportunity to realize photonic demultiplexer. For PCTIs with TM modes, we achieve second harmonic generation (SHG) through the interaction of multiband topological edge states by matching frequency ranges of these edge modes with fundamental and SH waves. This paper proposes a new approach for designing multiband PTCIs, which holds significant potential for the advancement of topological devices. These devices could be used in both linear and nonlinear multiband optical communications.
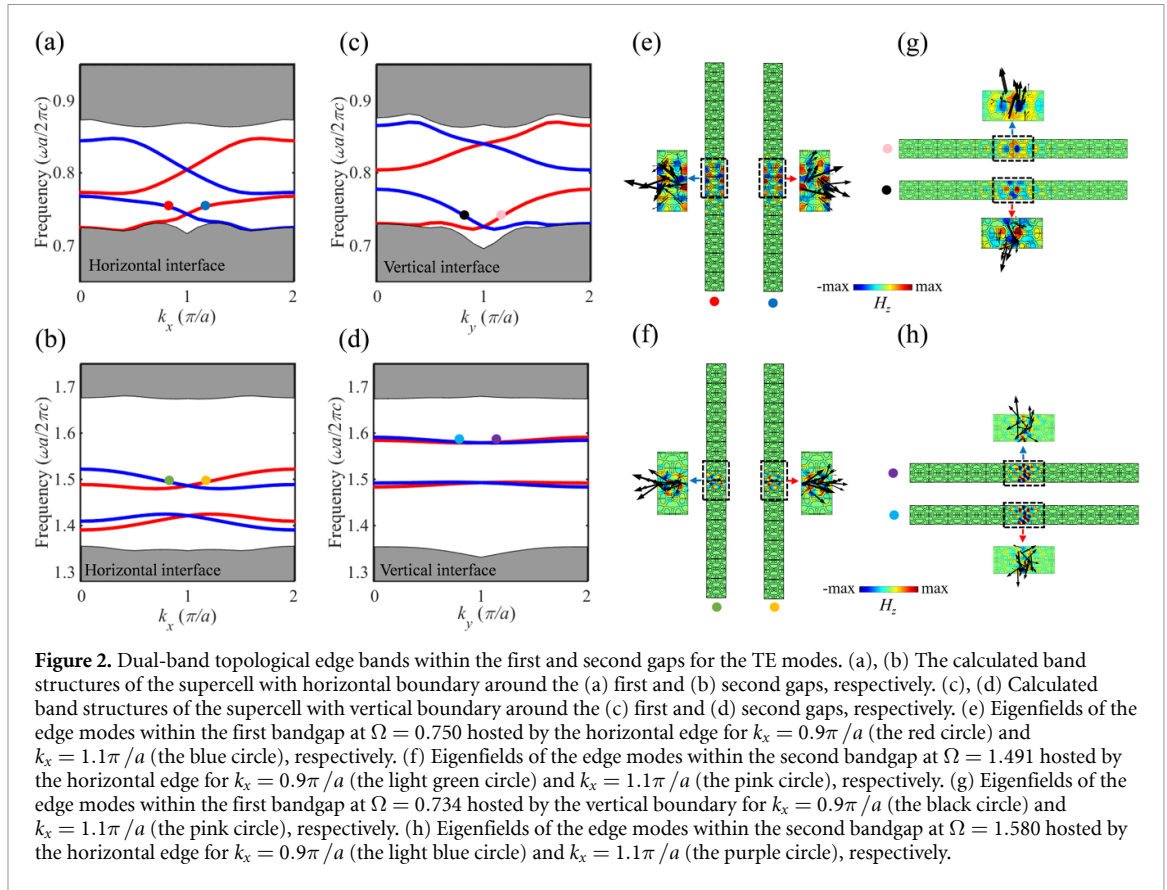
2. Multiband helical edge modes for the TE modes

We first consider the two-dimensional photonic system for the TE modes with out-of-plane magnetic fields. It is assumed that the PC is composed of dielectric materials with a permittivity value of 12. To design a dual-band PTCI, we impose glide and mirror symmetries on the PC, as implemented in previous works [19, 20, 32]. Next, we utilize the topology optimization method referenced in [28] to concurrently maximize the 8th- and 24th-order bandgaps. For the sake of simplicity, in this study, the frequency is normalized as $\Omega = \omega a/2\pi c$, with a representing the lattice constant and c denoting the speed of light in vacuum. As depicted in figure 1(a), the optimized PC, characterized by fully connected dielectric materials (yellow), can be easily produced using electron beam lithography technology and incorporated into optical circuits. Its band diagram in figure 1(b) reveals two bandgaps at the 8th- and 24th-orders, with frequency windows of (0.741, 0.887) and (1.372, 1.718), respectively. Due to the glide symmetry, the bands along the high symmetry line XM are degenerate [23]. Next, we pick two UCs from the optimized PC: the primitive UC (denoted as UCE1 within the red dashed box) and the other derived by horizontally translating UCE1 by a half-lattice constant (denoted as UCE2 within the black dashed box). Although UCE1 and UCE2 are selected from the same PC and thus share the same band diagram, their eigenmodes at the high symmetry point M have different parities. Figure 1(c) shows the eigenmodes at the M point of the 7th–8th bands (denoted by the black circle) and the 9th–10th bands (denoted by blue circle), i.e. the bands below and above the first (the 8th-order) bandgap, respectively, for UCE1 and UCE2. It can be seen that the two degenerate even modes with positive parities are below the two degenerate odd modes with negative parities for UCE1 while they are inverted for UCE2. Such band inversion can induce topological phase transition between UC1 and UC2 and further induce helical edge states at the interface between them [16–18]. Interestingly, apart from the band inversion between the 7th–8th bands and the 9th–10th bands for UCE1 and UCE2, there is also a band inversion between the 5th–6th bands (denoted by the red circle) and the 11th–12th bands (denoted by the pink circle), as shown in figure 1(d). For the second bandgap (the 24th-order), there are also two groups of band inversions between the odd and even modes at the M point, as shown in figures 1(e) and (f). Figure 1(e) shows that the two even modes of the 23rd–24th bands (denoted by the green circle) are below the two odd modes of the 25th–26th bands (denoted by the purple circle) for UCE1, while they are inverted for UCE2; figure 1(f) shows that the two odd modes of the 21st–22nd bands (denoted by the yellow circle) are below the two even modes of 27th–28th bands (denoted by the light blue circle) for UCE1, while they are inverted for UCE2. In fact, parities of eigenfields at M for the two degenerate bands are always opposite between UCE1 and UCE2. Therefore, when UCE1 and UCE2 are combined, a parity-inversion bandgap is formed. This leads to the appearance of topological edge states within the complete bandgap, as per the

Figure 1. The designed PC and its band structure for the TE modes. (a) The designed PC. UCE1 is the primitive UC and UCE2 is the translated UC. (b) The band structure of UCE1 and UCE2. (c) The eigenmodes at the *M* point of the 7th–8th bands (denoted by the black circle) and the 9th–10th bands (denoted by the blue circle). (d) The eigenmodes at the *M* point of the 5th–6th bands (denoted by the red circle) and the 11th–12th bands (denoted by the pink circle). (e) The eigenmodes at the *M* point of the 23rd-24th bands (denoted by the green circle) and the 25th–26th bands (denoted by the purple circle). (f) The eigenmodes at the *M* point of the 21st–22nd bands (denoted by the yellow circle) and the 27th–28th bands (denoted by the light blue circle).

Jackiw–Rebbi theory [33]. Furthermore, it is anticipated that several pairs of topological edge states will emerge within the bandgap when multiple parity-inversions occur beneath the bandgap.

In order to verify the presence of topological edge states, we create a supercell that consists of 6 UCE1s and 6 UCE2s, with an edge situated between them. Note that the configurations of horizontal and vertical edges formed between UCE1s and UCE2s are different, which can lead to different frequency ranges of the edge modes hosted by the two orthotropic edges. Here, we construct two supercells, each with horizontal and vertical edges between UCE1s and UCE2s, respectively. Figures 2(a) and (b) (figures 2(c) and (d)) show calculated band structures of the supercell with horizontal (vertical) edge around the first and second gaps, respectively. It is noticeable that within each bandgap, two pairs of helical edge modes appear for both horizontal and vertical edges, with each pair consisting of two bands of positive and negative group velocities crossing at $k_x = \pi/a$. Compared with traditional PTCIs that only host one group of gapped helical edge bands, two groups of helical edge bands are observed within each bulk gap herein, which is truly remarkable and can be attributed to the multiple parity-inversions of bulk bands below the bulk gap. For the horizontal boundary, the frequency ranges of the helical edge bands within the first gap are (0.731, 0.768) and (0.772, 0.847), and within the second gap are (1.391, 1.424) and (1.480, 1.522), respectively; for the vertical boundary, the frequency ranges of helical edge bands within the first gap are (0.730, 0.777) and (0.864, 0.870), and within the second bandgap are (1.484, 1.494) and (1.579, 1.591), respectively. Figure 2(e) (figure 2(g)) presents the eigenmodes at $\Omega = 0.750$ ($\Omega = 0.734$) of the edge bands within the first gap for the

Figure 2. Dual-band topological edge bands within the first and second gaps for the TE modes. (a), (b) The calculated band structures of the supercell with horizontal boundary around the (a) first and (b) second gaps, respectively. (c), (d) Calculated band structures of the supercell with vertical boundary around the (c) first and (d) second gaps, respectively. (e) Eigenfields of the edge modes within the first bandgap at $\Omega = 0.750$ hosted by the horizontal edge for $k_x = 0.9\pi/a$ (the red circle) and $k_x = 1.1\pi/a$ (the blue circle), respectively. (f) Eigenfields of the edge modes within the second bandgap at $\Omega = 1.491$ hosted by the horizontal edge for $k_x = 0.9\pi/a$ (the light green circle) and $k_x = 1.1\pi/a$ (the pink circle), respectively. (g) Eigenfields of the edge modes within the first bandgap at $\Omega = 0.734$ hosted by the vertical boundary for $k_x = 0.9\pi/a$ (the black circle) and $k_x = 1.1\pi/a$ (the pink circle), respectively. (h) Eigenfields of the edge modes within the second bandgap at $\Omega = 1.580$ hosted by the horizontal edge for $k_x = 0.9\pi/a$ (the light blue circle) and $k_x = 1.1\pi/a$ (the purple circle), respectively.

horizontal (vertical) boundary, and figure 2(f) (figure 2 (h)) presents the eigenmodes at $\Omega = 1.491$ ($\Omega = 1.580$) of the edge bands within the second gap for the horizontal (vertical) boundary, illustrating pronounced energy localization at the edge between UCE1 and UCE2. Meanwhile, the directional energy flux, depicted in the black dashed insets of figures 2(e)–(h) shows that the energy flux of these edge modes at $k_x = 0.9\pi/a$ and $k_x = 1.1\pi/a$ moves leftward (downward) and rightward (upward) for the horizontal (vertical) edge, respectively, indicative of finite orbital angular momentum (OAM) carried by these edge bands.

We next construct a metastructure comprising UCE1s and UCE2s, separated by a horizontal channel, to investigate the transmission characteristics of the helical edge modes, as depicted in figure 3(a). We excite the edge modes by using a source positioned at the left end of the channel. The transmission ratios displayed in figures 3(b) and (c) highlight enhanced transmission within the frequency ranges corresponding to the helical edge states within both two gaps, as shaded by pink and blue colors, respectively. A hallmark feature of helical edge states is the pseudospin-locked one-way propagation property. To demonstrate this phenomenon, we employ a quartet of antennas (as outlined in [18].) at the midpoint of the interface to launch waves with either positive or negative OAM, thereby exciting the corresponding pseudospin-locked edge states. The resultant magnetic field intensities, as captured in figures 3(d) and (e) (first bandgap) and figures 3(f) and (g) (second bandgap), demonstrate that waves carrying positive OAM propagate rightward, whereas those carrying negative OAM propagate leftward, affirming the pseudospin-locked unidirectional transmission feature of the helical edge modes within both two bandgaps.

Leveraging the mismatched frequency ranges of helical edge modes hosted by two orthogonal interfaces, we create an optical demultiplexer, as sketched in figure 4(a), which consists of 6×6 UCE1s encapsulated by four layers of UCE2s extending to the left and below, wherein horizontal (red) and vertical (blue) edges are formed between UCE1s and UCE2s. We place a point source, denoted by the yellow sphere, place at the corner formed between UCE1s and UCE2s. Figures 4(b)–(d) demonstrate the demultiplexing capability of the device: at $\Omega = 0.76$, waves propagate along both edges (figure 4(b)); at $\Omega = 1.407$, the propagation is confined to the horizontal edge (figure 4(c), and at $\Omega = 1.583$, it is restricted to the vertical edge (figure 4(d)). This precise control over wave propagation underscores the potential of the device to spatially route signals based on frequency in integrated photonic circuits.
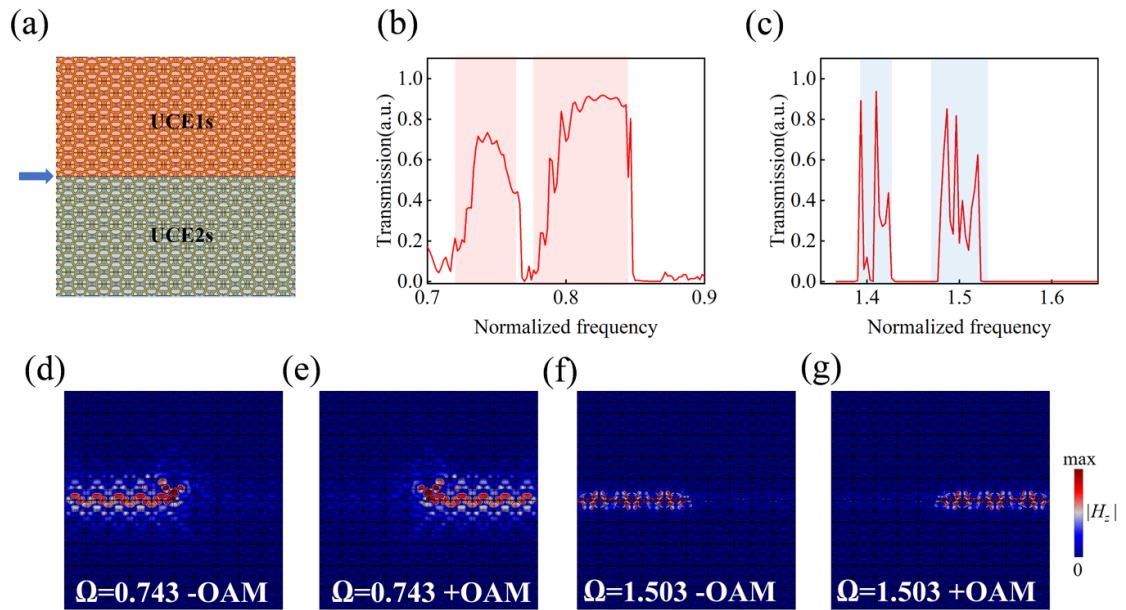
Figure 3. Propagation properties of dual-band helical edge states within two gaps. (a) Schematic of the metastructure for demonstrating the transmission property of the helical edge modes. (b), (c) The transmission ratios of waves that propagate along the channel around the (b) first and (c) second gaps, respectively. (d), (e) Leftward and rightward unidirectional propagations of waves carrying (d) negative and (e) positive OAMs under $\Omega = 0.743$, respectively. (f), (g) Leftward and rightward unidirectional propagations of waves carrying (f) negative and (g) positive OAMs under $\Omega = 1.503$, respectively.
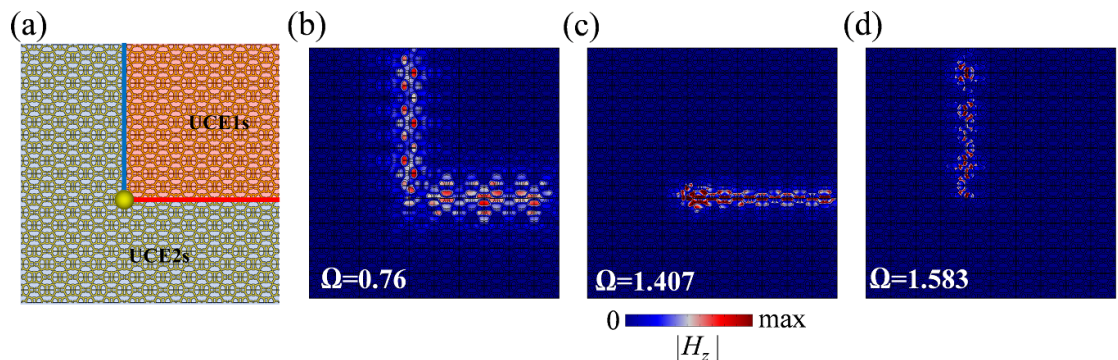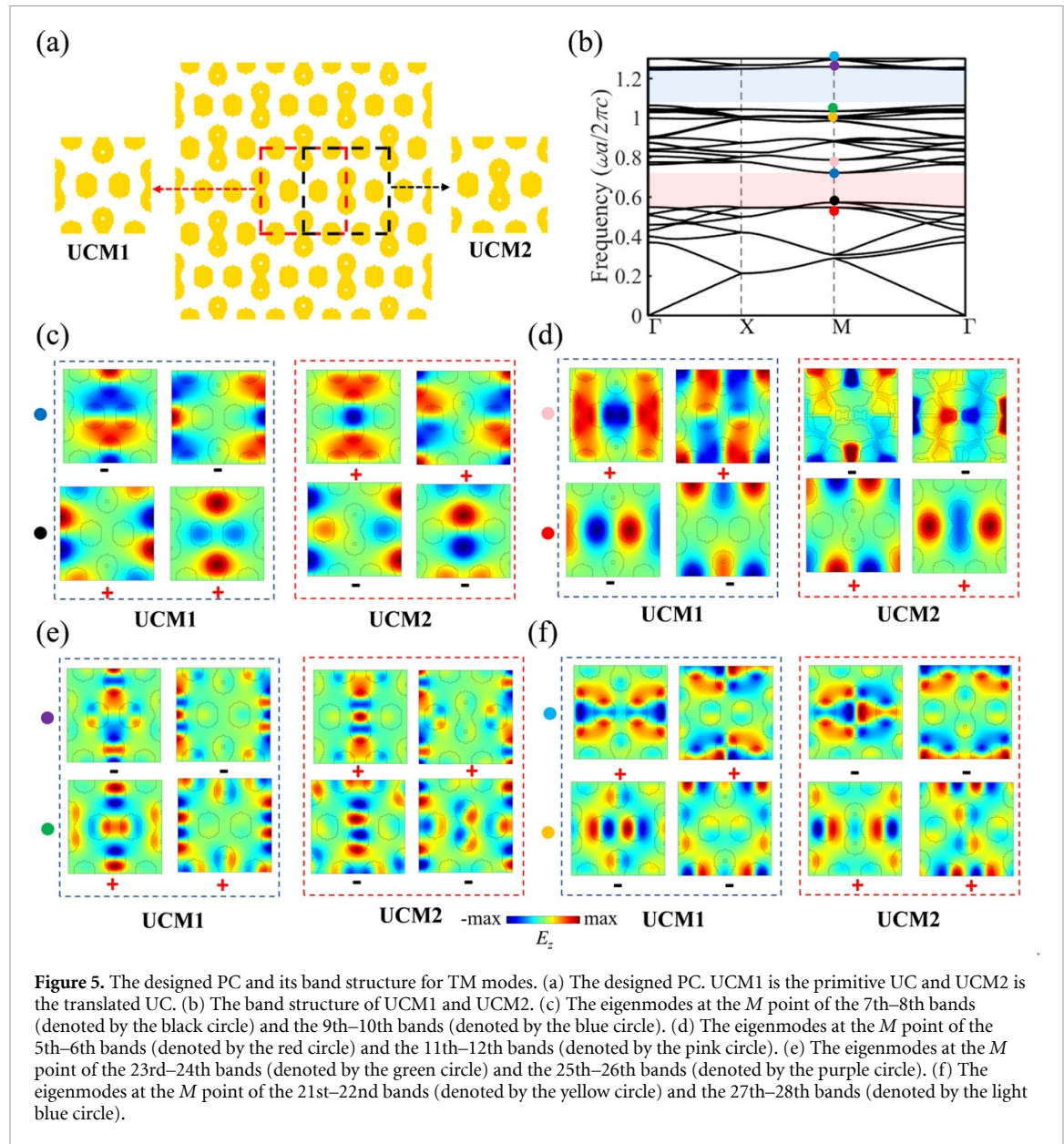

Figure 4. Optical demultiplexer of helical edge states. (a) The prototype of the optical demultiplexer. (b)–(d) Normalized magnetic field distributions at the frequency of (b) $\Omega = 0.76$, (c) $\Omega = 1.407$, (d) $\Omega = 1.583$, respectively.
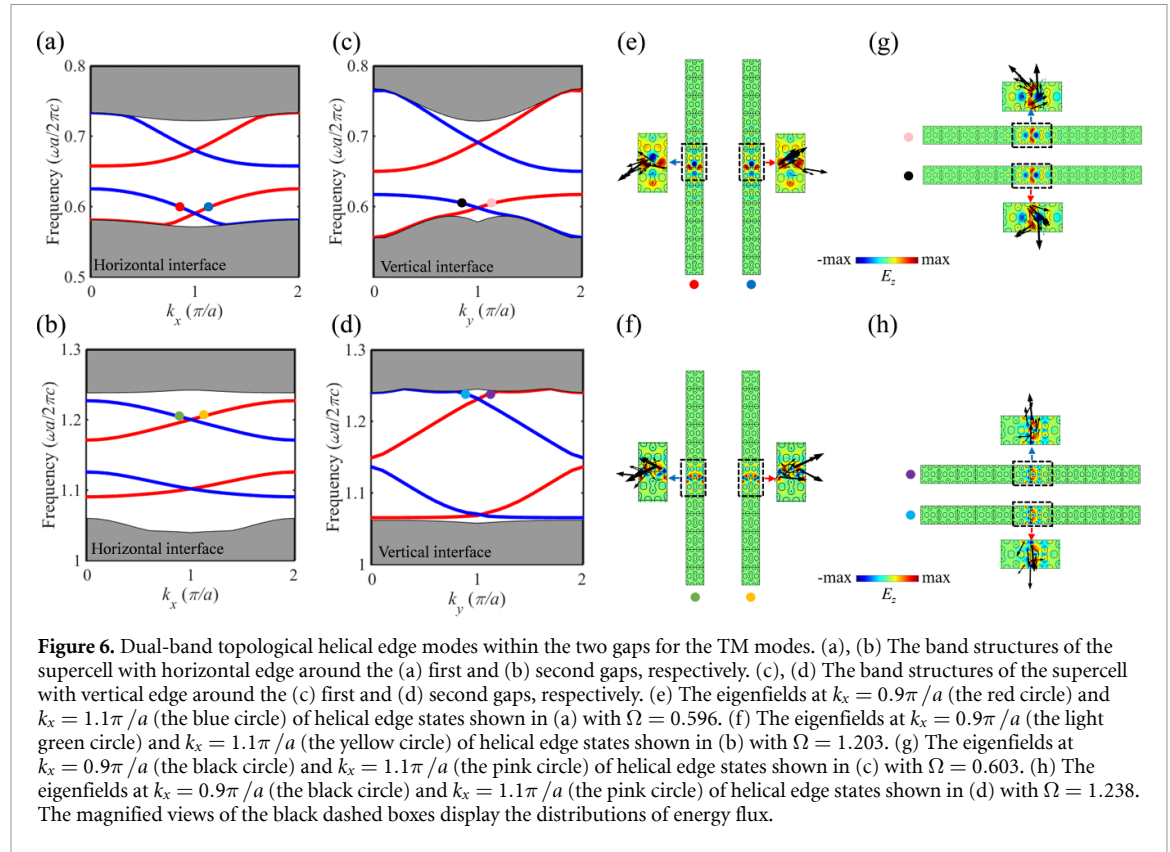
3. Multiband helical edge states for the TM modes

In this section, we further design the multiband PTCI for the TM modes and demonstrate the nonlinear SHG via the interaction of multiband helical edge states. Adhering to the *p4mm* symmetry constraint, we employ a topology optimization method (as detailed in [34]) to concurrently maximize the minimal imaginary parts of wave vectors at $\Omega = 0.6$ and $\Omega = 1.2$. As a result, two distinct bandgaps situated around the two specific frequencies are formed. The optimized PC is depicted in figure 5(a), with its band diagram illustrated in figure 5(b). It can be seen that two bandgaps, namely the 8th- and 24th-orders, are obtained, for which the frequency windows are (0.573, 0.723) and (1.064, 1.245), respectively. Next, we pick two UCs from this PC: UCM1 (the primitive UC within the red box) and UCM2 (derived from UCM1 by a half-lattice constant horizontal translation and marked by the black dashed box). Figures 5(c) and (d) demonstrate eigenfields at *M* for two pairs of bands beneath the first and second bandgaps, respectively. Similar to the TE modes, there are also two groups of band inversions between odd and even modes at the *M* point between UCM1 and UCM2 for both the first and second bandgaps, as shown in figures 5(c)–(f). For the first bandgap (the 8th-order bandgap), figure 5(c) shows that the two even modes of the 7th–8th bands (denoted by the black circle) are below the two odd modes of the 9th–10th bands (denoted by the blue circle) for UCM1, while they are inverted for UCM2; figure 5(d) shows that the two odd modes of the 5th–6th bands (denoted by the red

Figure 5. The designed PC and its band structure for TM modes. (a) The designed PC. UCM1 is the primitive UC and UCM2 is the translated UC. (b) The band structure of UCM1 and UCM2. (c) The eigenmodes at the *M* point of the 7th–8th bands (denoted by the black circle) and the 9th–10th bands (denoted by the blue circle). (d) The eigenmodes at the *M* point of the 5th–6th bands (denoted by the red circle) and the 11th–12th bands (denoted by the pink circle). (e) The eigenmodes at the *M* point of the 23rd–24th bands (denoted by the green circle) and the 25th–26th bands (denoted by the purple circle). (f) The eigenmodes at the *M* point of the 21st–22nd bands (denoted by the yellow circle) and the 27th–28th bands (denoted by the light blue circle).
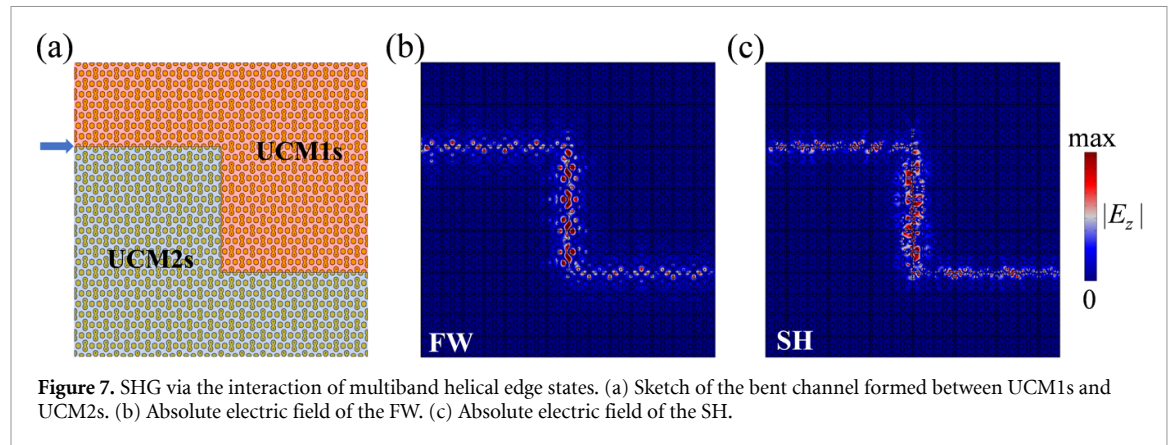
circle) are below the two even modes of the 11th–12th bands (denoted by the purple circle) for UCM1, while they are inverted for UCM2. For the second bandgap (the 24th-order), figure 5(e) shows that the two even modes of the 23rd–24th bands (denoted by the green circle) are below the two odd modes of the 25th–26th bands (denoted by the purple circle) for UCM1, while they are inverted for UCM2; figure 5(f) shows that the two odd modes of the 21st–22nd bands (denoted by the yellow circle) are below the two even modes of the 27th–28th bands (denoted by the light blue) for UCM1, while they are inverted for UCM2. Therefore, it is predicted that two pairs of QSHE-based edge states may emerge within both the first and second bandgaps.

To further validate multiple topological edge states for the TM modes, we build two supercells consisting of 6 UCM1s and 6 UCM2s with horizontal and vertical edges, respectively. Figures 6(a)–(d) demonstrate calculated band structures of the supercell with horizontal (vertical) edge around the first and second gaps, respectively. We can observe that, for both horizontal and vertical edges, two groups of topological edge modes appear within both gaps and each group of edge modes include two edge bands of opposite group velocities that cross at $k_x = \pi/a$. For the horizontal edge, the frequency ranges of the two pairs of helical edge modes within the first gap are (0.581, 0.626) and (0.658, 0.722), respectively, while they are (1.091, 1.126) and (1.171, 1.227) within the second gap, respectively. For the vertical edge, the frequency ranges of the two pairs of edge modes within the first gap are (0.586, 0.617) and (0.650, 0.721), respectively, while they are (1.065, 1.136) and (1.150, 1.241) within the second bandgap, respectively. Figure 6(e) (figure 6(g)) illustrates eigenfields at $k_x = 0.9\pi/a$ and $k_x = 1.1\pi/a$ of helical edge modes with $\Omega = 0.596$ ($\Omega = 0.603$) hosted by the

Figure 6. Dual-band topological helical edge modes within the two gaps for the TM modes. (a), (b) The band structures of the supercell with horizontal edge around the (a) first and (b) second gaps, respectively. (c), (d) The band structures of the supercell with vertical edge around the (c) first and (d) second gaps, respectively. (e) The eigenfields at $k_x = 0.9\pi/a$ (the red circle) and $k_x = 1.1\pi/a$ (the blue circle) of helical edge states shown in (a) with $\Omega = 0.596$. (f) The eigenfields at $k_x = 0.9\pi/a$ (the light green circle) and $k_x = 1.1\pi/a$ (the yellow circle) of helical edge states shown in (b) with $\Omega = 1.203$. (g) The eigenfields at $k_x = 0.9\pi/a$ (the black circle) and $k_x = 1.1\pi/a$ (the pink circle) of helical edge states shown in (c) with $\Omega = 0.603$. (h) The eigenfields at $k_x = 0.9\pi/a$ (the black circle) and $k_x = 1.1\pi/a$ (the pink circle) of helical edge states shown in (d) with $\Omega = 1.238$. The magnified views of the black dashed boxes display the distributions of energy flux.

horizontal (vertical) edge, corresponding to colorful circles in figures 6(a), (c), (e) and (g) illustrates eigenfields at $k_x = 0.9\pi/a$ and $k_x = 1.1\pi/a$ of helical edge modes with $\Omega = 1.203$ ($\Omega = 1.238$) hosted by the horizontal (vertical) edge, corresponding to colorful circles in figures 6(b) and (d). We can find that energies are intensely concentrated at the edge between UCM1s and UCM2s. Meanwhile, from the energy flux distributions shown in figures 6(e)–(h), it can be observed that energies of these helical edge modes, hosted by the horizontal (vertical) edge, at $k_x = 0.9\pi/a$ and $k_x = 1.1\pi/a$ flow leftward (downward) and rightward (upward), respectively, indicative of finite OAM carried by these states.

According to frequency ranges of the helical edge modes within both the first and second gaps, we can find a notable characteristic: the frequency range of the second group of helical edge modes within the second gap is nearly double that of the first group within the first bandgap, for both horizontal and vertical edges. Hence, we can leverage this unique property to achieve topologically protected nonlinear SHG by matching the first group of helical edge modes within the first gap for the fundamental wave (FW) and the second group of helical edge modes in the second gap for the SH. To demonstrate the SHG via the interaction of the two groups of helical edge modes, we set the lattice constant of the UC as 939.45 nm and assign the second-order nonlinear susceptibility of $\chi^{(2)} = 10^{-21} \text{CV}^{(-2)}$ to the dielectric materials. Then, we construct a bent channel between UCM1s and UCM2s, as illustrated in figure 7(a), and launch a point source with wavelength of 1550 nm ($\Omega = 0.606$), as denoted by the blue arrow. Figure 7(b) shows the normalized electric field of the FW, from which we can see that the FW propagates along the bent channel effectively. Crucially, via the interaction of FW and the nonlinear dielectric materials, SH can be generated. As the frequency of SH locates within the frequency range of the second group of helical edge modes within the second gap, the SH is also highly localized along the bent channel, as evidenced in figure 7(c). Apart from demonstrating the SHG phenomenon, we also calculate the normalized nonlinear overlap factor of the edge modes for FW and SH, defined by $\beta = \frac{\left| \int E_z^{\text{FW}} E_z^{\text{FW}} \left(E_z^{\text{SH}} \right)^* \text{d}V \right|}{\sqrt{\int |E_z^{\text{FW}} E_z^{\text{FW}}|^2 \text{d}V} \sqrt{\int |E_z^{\text{SH}}|^2 \text{d}V}}$, and the nonlinear SHG efficiency, defined by $\rho_{\text{SH}} = \frac{P_{\text{SH}}}{P_{\text{FW}}^2}$, where E_z^{FW} and E_z^{SH} represent the electric fields of edge modes for FW and SH, P_{FW} and P_{SH} are the power of the FW and SH, respectively [35–37]. The calculated normalized nonlinear overlap factor of the edge modes for FW ($\Omega = 0.606$) and SH is 0.0043. The nonlinear SHG efficiency at $\Omega = 0.606$ is 3.1×10^{-8}. We note that for experimental implementations and observations of SHG in the proposed structure, many semiconductor materials with similar permittivity as used above in the theoretical analysis, such as GaAs and AlGaAs, can be employed.

Figure 7. SHG via the interaction of multiband helical edge states. (a) Sketch of the bent channel formed between UCM1s and UCM2s. (b) Absolute electric field of the FW. (c) Absolute electric field of the SH.

4. Conclusions

In summary, we have designed PTCIs that support multiband helical edge states for TM and TE modes, respectively. These PTCIs feature with two bulk gaps and possess two groups of helical edge modes within each gap, having promising potentials in multiband optical signal processing and communication applications. For PTCIs with TE modes, leveraging the mismatched frequency ranges of the helical edge modes at two orthogonal edges, we have created a topological photonic demultiplexer, paving the way for designing on-chip topological optical demultiplexing devices. For PTCIs with TM modes, by aligning the frequency ranges of the helical edge modes within the first and second gaps with FW and SH, respectively, we have demonstrated SHG via the interaction of helical edge states, which holds significant promise for developing topologically protected nonlinear optical devices.

Data availability statement

All data that support the findings of this study are included within the article (and any supplementary files).

Acknowledgments

ORCID iDs

Yafeng Chen ⬚ https://orcid.org/0000-0002-5459-4428
Zhihao Lan ⬚ https://orcid.org/0000-0002-1322-5925

References

[1] Lu L, Joannopoulos J D and Soljačić M 2014 *Nat. Photonics* **8** 821
[2] Khanikaev A B and Shvets G 2017 *Nat. Photonics* **11** 763
[3] Wang H-X and Jiang J-H 2022 *Front. Phys.* **10** 866552
[4] Ma T and Shvets G 2016 *New. J. Phys.* **18** 025012
[5] Xi X, Li X-M, Ye K-P, Wu H-B, Chen J and Wu R-X 2021 *New. J. Phys.* **23** 083042
[6] Jana S, Devi K M, Kulkarni G, Mallick S and Chowdhury D R 2023 *New. J. Phys.* **25** 093023
[7] Ozawa T *et al* 2019 *Rev. Mod. Phys.* **91** 015006
[8] Rao M, Shi F, Rao Z, Yang J, Song C, Chen X, Dong J, Yu Y and Yu S 2024 *Light Sci. Appl.* **13** 19
[9] Tang G-J *et al* 2024 *Light Sci. Appl.* **13** 166
[10] Smirnova D, Leykam D, Chong Y and Kivshar Y 2020 *Appl. Phys. Rev.* **7** 021306
[11] Zhuang Z-P, Zeng H-L, Chen X-D, He X-T and Dong J-W 2024 *Phys. Rev. Lett.* **132** 113801
[12] Wang Z, Chong Y, Joannopoulos J D and Soljačić M 2009 *Nature* **461** 772
[13] Wang Z, Chong Y, Joannopoulos J D and Soljačić M 2008 *Phys. Rev. Lett.* **100** 013905
[14] He X-T, Liang E-T, Yuan -J-J, Qiu H-Y, Chen X-D, Zhao F-L and Dong J-W 2019 *Nat. Commun.* **10** 872
[15] Liu J-W, Shi F-L, He X-T, Tang G-J, Chen W-J, Chen X-D and Dong J-W 2021 *Adv. Phys.* X **6** 1905546
[16] Wu L-H and Hu X 2015 *Phys. Rev. Lett.* **114** 223901
[17] Xu L, Wang H-X, Xu Y-D, Chen H-Y and Jiang J-H 2016 *Opt. Express* **24** 18059
[18] Yang Y, Xu Y F, Xu T, Wang H-X, Jiang J-H, Hu X and Hang Z H 2018 *Phys. Rev. Lett.* **120** 217401

[19] Zhang X, Wang H-X, Lin Z-K, Tian Y, Xie B, Lu M-H, Chen Y-F and Jiang J-H 2019 *Nat. Phys.* **15** 582
[20] Zhang L, Yang Y, Lin Z K, Qin P, Chen Q, Gao F and Chen H 2020 *Adv. Sci.* **7** 1902724
[21] Wang H-X, Chen Y, Hang Z H, Kee H-Y and Jiang J-H 2017 *npj Quantum Mater.* **2** 54
[22] Wang H-X, Chen Y, Hang Z H, Kee H-Y and Jiang J-H 2022 *npj Quantum Mater.* **2** 54
[23] Chen Y, Wang H-X, Lan Z and Su Z 2024 *Phys. Rev. B* **109** 075132
[24] Xie B, Wang H-X, Zhang X, Zhan P, Jiang J-H, Lu M and Chen Y 2021 *Nat. Rev. Phys.* **3** 1
[25] Xie B, Su G, Wang H-F, Liu F, Hu L, Yu S-Y, Zhan P, Lu M-H, Wang Z and Chen Y-F 2020 *Nat. Commun.* **11** 3768
[26] Xie B-Y, Wang H-F, Wang H-X, Zhu X-Y, Jiang J-H, Lu M-H and Chen Y-F 2018 *Phys. Rev. B* **98** 205147
[27] Xie B-Y, Su G-X, Wang H-F, Su H, Shen X-P, Zhan P, Lu M-H, Wang Z-L and Chen Y-F 2019 *Phys. Rev. Lett.* **122** 233903
[28] Chen Y, Lan Z and Zhu J 2022 *Nanophotonics* **11** 1345
[29] Chen Q, Zhang L, He M, Wang Z, Lin X, Gao F, Yang Y, Zhang B and Chen H 2019 *Adv. Opt. Mater.* **7** 1900036
[30] Lan Z, You J W, Ren Q, Sha W E I and Panoiu N C 2021 *Phys. Rev. A* **103** L041502
[31] Kim K H and Om K K 2021 *Adv. Opt. Mater.* **9** 2001865
[32] Lin Z-K, Wang H-X, Xiong Z, Lu M-H and Jiang J-H 2020 *Phys. Rev. B* **102** 035105
[33] Jackiw R and Rebbi C 1976 *Phys. Rev. D* **13** 3398
[34] Chen Y, Lan Z and Zhu J 2022 *Phys. Rev. Appl.* **17** 054003
[35] Carletti L, Locatelli A, Stepanenko O, Leo G and De Angelis C 2015 *Opt. Express* **20** 26544
[36] Zanotti S, Minkov M, Fan S, Andreani L C and Gerace D 2021 *Nanomaterials* **11** 605
[37] Medina-Vázquez J A, E Y González-Ramírez and J G Murillo-Ramírez 2023 *J. Condens. Matter Phys.* **35** 385401